

CHANG-ES. XXX. 10 kpc Radio Lobes in The Sombrero Galaxy

YANG YANG,¹ JIANG-TAO LI,¹ THERESA WIEGERT,² ZHIYUAN LI,^{3,4} FULAI GUO,^{5,6} JUDITH IRWIN,⁷ Q. DANIEL WANG,⁸
RALF-JUERGEN DETTMAR,⁹ RAINER BECK,¹⁰ JAYANNE ENGLISH,¹¹ AND JI LI¹

¹*Purple Mountain Observatory, Chinese Academy of Sciences, 10 Yuanhua Road, Nanjing 210023, People's Republic of China*

²*Instituto de Astrofísica de Andalucía (IAA-CSIC), Glorieta de la Astronomía s/n, 18008 Granada, Spain*

³*School of Astronomy and Space Science, Nanjing University, Nanjing 210023, People's Republic of China*

⁴*Key Laboratory of Modern Astronomy and Astrophysics, Nanjing University, Nanjing 210023, People's Republic of China*

⁵*Key Laboratory for Research in Galaxies and Cosmology, Shanghai Astronomical Observatory, Chinese Academy of Sciences, 80 Nandan Road, Shanghai 200030, People's Republic of China*

⁶*University of Chinese Academy of Sciences, 19A Yuquan Road, Beijing 100049, People's Republic of China*

⁷*Dept. of Physics, Eng. Phys. & Astronomy, Queen's University, Kingston, Canada, K7L 3N6*

⁸*Department of Astronomy, University of Massachusetts, North Pleasant Street, Amherst, MA 01003-9305, USA, LGRT-B 619E, 710*

⁹*Ruhr University Bochum, Faculty of Physics and Astronomy, Astronomical Institute (AIRUB), 44780 Bochum, Germany*

¹⁰*Max-Planck-Institut für Radioastronomie, Auf dem Hügel 69, 53121, Bonn, Germany*

¹¹*Dept. of Physics & Astronomy, University of Manitoba, Winnipeg, Manitoba, R3T 2N2*

ABSTRACT

We report the discovery of the 10 kilo-parsec (kpc) scale radio lobes in the Sombrero galaxy (NGC 4594), using data from the Continuum Halos in Nearby Galaxies—an Expanded Very Large Array (VLA) Survey (CHANG-ES) project. We further examine the balance between the magnetic pressure inside the lobes and the thermal pressure of the ambient hot gas. At the radii r of $\sim (1 - 10)$ kpc, the magnetic pressure inside the lobes and the thermal pressure of the ambient hot gas are generally in balance. This implies that the jets could expand into the surroundings at least to $r \sim 10$ kpc. The feedback from the active galactic nucleus (AGN) jet responsible for the large-scale lobes may help to explain the unusually high X-ray luminosity of this massive quiescent isolated disk galaxy, although more theoretical work is needed to further examine this possibility.

Keywords: galaxies: individual (M104, or NGC 4594)— Jet(?) — magnetic fields(?) — radio continuum: galaxies

1. INTRODUCTION

Collimated jets and associated large-scale coherent structures carry a significant amount of energy outwards from the accreting super-massive black hole (SMBH) in the galactic nucleus. This energy is injected into the interstellar medium (ISM) or the circumgalactic medium (CGM) in the form of mechanical, thermal, cosmic ray (CR), and magnetic energy (Guo et al. 2018; Harrison et al. 2018; Hardcastle 2018; Kormendy & Ho 2013). The X-ray bubble/cavity enveloping the radio jet is direct observational evidence of the interaction between the jet and the surrounding gas. However, most X-ray cav-

ities are detected in massive galaxy clusters where the gas density is high (McNamara & Nulsen 2007). Deep insights into an isolated ¹ galaxy hosting radio jets could complement our current understanding to the physical processes of jet feedback by AGN in different environments. For example: How large is the sphere of influence of the jets? Is there a balance between the magnetic pressure and the hot gas thermal pressure? How much mechanical energy is carried out by the jets? Do the radio jets have enough power to heat the ambient hot gas?

¹ The definition of “isolated” is based on the “local galaxy number density” $\rho \leq 0.6$. (Li & Wang 2013a).

The Sombrero galaxy (NGC 4594 or M104), at a distance of $d \sim 9.5 \text{ Mpc}^2$ (McQuinn et al. 2016), is the most massive disk galaxy at $d \lesssim 30 \text{ Mpc}$. The galaxy has a stellar mass of $M_* \sim 10^{11.3} M_\odot$ (Kennicutt et al. 2011) and an unusually high rotation velocity of $v_{\text{rot}} \sim 379 \text{ km s}^{-1}$ (Jiang et al. 2023), inferring a total halo mass of $M_{\text{h}} \sim 10^{13} M_\odot$ (Karachentsev et al. 2020). The galaxy is isolated in the field with no massive companions, and the star formation (SF) is quite inactive (with a rate of $\text{SFR} \sim 0.4 M_\odot \text{ yr}^{-1}$). On the other hand, its X-ray emission is unusually high compared to similarly massive or SF inactive disk galaxies (Li J. et al. 2011; Li & Wang 2013a,b). The Sombrero hosts a SMBH with a mass of $M_{\text{SMBH}} \sim 10^9 M_\odot$ (Kormendy 1988; Kormendy et al. 1996) and a low Eddington ratio of $L_{\text{bol}}/L_{\text{Edd}} \sim 10^{-5}$ (Kharb et al. 2016). Existing multi-wavelength observations reveal a compact X-ray and radio core and bipolar sub-parsec (pc)- and pc-scale jets at different radio frequencies (Hada et al. 2013; Mezcuca & Prieto 2014; Gallimore et al. 2006), but there is no previous evidence of large-scale coherent structures of these radio jets.

In this paper, we present the results from our latest VLA observations of the Sombrero galaxy, which are obtained from the Continuum Halos in Nearby Galaxies—an Expanded Very Large Array Survey project (CHANG-ES, Irwin et al. 2012a,b). We present our observations and data reduction in §2, the key results in §3, and the scientific discussion and concluding remarks in §4.

2. OBSERVATIONS AND DATA REDUCTION

The VLA radio continuum data of the Sombrero galaxy (project ID:10C-119) are taken in the B, C, and D configurations in L-band (center frequency 1.5 GHz, bandwidth 512 MHz), and in C and D configurations in C-band (center frequency 6 GHz, bandwidth 2 GHz). All polarization products (Stokes I, Q, U and V) were obtained. Further details of these VLA observations are listed in Table 1.

We reduced the VLA data using the Common Astronomy Software Applications package (CASA, version 4.5) following standard procedures. Each individual visibility set was flagged, calibrated, imaged and restored. We further inspected all visibility data by eye, and manually flagged bad data (caused by radio frequency interference and instrumental effects). The Stokes I images were then produced using the CLEAN task, with the Multi-frequency Synthesis mode, $n_{\text{terms}} = 2$, and Briggs

robust 0 weighting. The CASA WIDEBANDPBCOR task was used to carry out wide-band primary beam corrections. Flux measurements were made from the primary beam-corrected images in all cases. All measured results are listed in Table 1. The root-mean-square error (RMS) is measured in a signal-free portion (near the source) of each image. The uncertainty of the flux densities for each region was calculated using the equation $\sigma \simeq \sqrt{N_b \times RMS^2 + (\eta \times S)^2}$, where N_b corresponds to the number of synthesized beams, and η is a factor to account for uncertainties in the calibration system, which we adopted as $\eta = 0.03$ for the VLA radio images (Perley & Butler 2013); S is the flux density of the core, and we measured this by fitting a Gaussian to the nuclear region in each image with the IMFIT task. The fitting region is approximately twice the full-width-half-maximum of the synthesized beam.

Stokes Q and U maps were produced using the same sets of input parameters as the total intensity images. We derived the linearly polarized intensity image using the relation $P = \sqrt{Q^2 + U^2 - \sigma_{Q,U}^2}$, where $\sigma_{Q,U}$ is the RMS noise in the Q and U maps. The polarization angle of the observed electric vector (χ) is given by $\chi = 1/2 \arctan(U/Q)$; and the perpendicular direction of χ represents the apparent magnetic field orientation on the sky plane. However, we have not corrected for any potential Faraday rotation yet.

3. RESULTS

Our derived radio intensity map is shown in Figure 1. In the deep VLA L-band (1.5 GHz) D-configuration total intensity image (Figure 1a), we for the first time detect the galactic scale bipolar radio lobes extending to $\sim 10 \text{ kpc}/7 \text{ kpc}$ north and south of the disk. These FR I-like³ bipolar lobes are oriented almost perpendicular to the galactic disk (with P.A.⁴ $\sim -10^\circ$). With the higher resolution 1.5 and 6 GHz images, we also detect some possibly coherent smaller scale (a few hundred pc to a few kpc) features of these large-scale radio lobes, with a slightly different P.A. of $\sim -20^\circ$ (Figure 2). Radio jets on a similar kpc or even smaller scales have been detected by several authors. Hada et al. (2013) detected the sub-pc scale bipolar jets in Sombrero at different frequencies (1.4, 2.3, 5.0, 8.4, 15.2, 23.8, and

³ FR I galaxies have a “fan-shaped” radio morphology, with diffuse and gradually diminishing radio jets. FR II galaxies have more powerful and collimated radio jets extending over greater distances, terminating in bright “hotspots” at the outer edges of the radio lobes (Fanaroff & Riley 1974).

⁴ P.A. is the position angle, the direction perpendicular to the galactic disk is defined as 0° .

² This distance is updated from the previous CHANG-ES standard of 12.7 Mpc (Wiegert et al. 2015).

43.2 GHz) with the VLBI, which has a P.A. of $\sim -20^\circ$. Mezcua & Prieto (2014) resolved a pc-scale jet into several components at 23.8 GHz with the VLBI with a P.A. $\sim -31^\circ$. Gallimore et al. (2006) detected a fainter kpc-scale (3.8 kpc) linear radio structure with archival VLA 5-GHz observations.

We then calculate the in-band spectral index α of the bipolar radio lobes, which is defined as $S \propto \nu^\alpha$ (Wiegert et al. 2015). As shown in Figure 1d, the northern (southern) lobe has an average L-band spectral index of $\alpha_{1.5} = -1.5 \pm 0.9$ (-1.2 ± 1.0). For comparison, the mean spectral index of the compact core is $\sim 0.3 \pm 0.1$. Our multi-band, multi-configuration CHANG-ES data allow us to calculate the band-to-band spectral index using images with comparable angular resolution, such as $\alpha_{\text{BL-CC}}$ (B-configuration L-band to C-configuration C-band spectral index). Irwin et al. (2019) reported a similarly flat radio spectrum from the core of the Sombrero galaxy ($\alpha_{\text{BL-CC}} = 0.43 \pm 0.01$, $\alpha_{\text{CL-DC}} = 0.07 \pm 0.03$), which is in general consistent with the in-band spectral index reported here. Because of the difficulty in subtracting the artificial effects produced by the bright central core from the extended features with the high-resolution data, we do not measure the band-to-band spectral index of the bipolar lobes. However, it is clear that there is a significant steepening of the radio spectra from the core to the larger scale structures (Figure 1d).

Figure 1c shows the linear polarization map obtained from our D-configuration L-band data, the map is superimposed with the magnetic field orientations and Stokes I contours. The vertically oriented cylindrical structure along the jet axis reveals the bipolar polarization lobes, which is AGN related (Yang et al. 2022). These polarization segments are perpendicular to the bipolar polarization lobes, indicating the presence of a helical/toroidal magnetic field component traveling outward with the jet. Additionally, the map reveals a dissociated feature with enhanced polarization emission at the endpoint of the northern lobe. At 1.5 GHz, the average fractional polarization of this feature is approximately $\sim 50\%$, compared to $\sim 1\%$ of the core. Besides the polarization core, we have not detected the bipolar polarization lobes in the better-resolution 1.5 and 6-GHz images.

4. DISCUSSION AND CONCLUSIONS

The Sombrero galaxy is unusually X-ray bright compared to other disk galaxies with comparable mass and/or SFR (Li Z. et al. 2011; Li J. et al. 2011; Li & Wang 2013a,b). The unresolved X-ray emission is significantly beyond the stellar content (Figure 1b), indicating the presence of extended hot CGM. We then want

to examine how this enhanced hot gas X-ray emission is impacting or being impacted by the jets on different scales. The first thing we want to examine is the balance between the thermal pressure of the hot gas and the pressure of the magnetic field frozen in the radio lobes, as revealed in the polarization map (Figure 1c).

We estimate the magnetic field strength B_{eq} from the synchrotron emission of the radio lobe, based on the assumption of equipartition between the energy densities of the CRs and that of the magnetic field. This assumption is premised on an ideal scenario that CRs and magnetic fields are strongly coupled and exchange energy until equilibrium is reached over a sufficient propagation time scale and length scale (typically ~ 1 kpc; e.g., Seta & Beck 2019). We use the revised equipartition formula of Beck & Krause (2005) to calculate B_{eq} at different places of the radio lobes. Here we assume the number density ratio of the CR proton and electron to be $K = 100$, and use the corresponding in-band spectral index (in Table 2) of the hundreds-pc, sub-kpc, and kpc scale regions, as labelled in Figures 1 and 2. In addition, the path lengths through the emitting medium along the line of sight are assumed to be equal to the width of the extended radio structures on the sky plane. Derived B_{eq} values of different extended radio structures are listed in Col. 7 of Table 2. The B_{eq} of the kpc and hundreds-pc scale regions are typically 5-7 μG and 26-51 μG , respectively. The number density ratio K is expected to increase with increasing distance from the injection sites of CRs due to the much more severe energy losses of electrons than protons. Our measured B_{eq} would be underestimated by a factor of $(K_{\text{real value}}/K)^{1/(3+\alpha)}$, but the equipartition magnetic pressure, $P_B = B_{\text{eq}}^2/8\pi$, is not very sensitive to K . Krause et al. (2006) estimated B_{eq} of NGC 4594, using the same method and assumptions as we used. They obtained an average B_{eq} of $4 \pm 1 \mu\text{G}$ over the entire galaxy excluding the nucleus, which is consistent with our measurements of the kpc-scale lobes.

We also calculate the equipartition magnetic pressure $P_B = B_{\text{eq}}^2/8\pi$ and the synchrotron half-power lifetime of CR electrons t_{syn} (using B_{eq} and the center frequency of the corresponding band; Beck & Wielebinski 2013), which are listed in Col. 8 and 9 of Table 2. The typical value of t_{syn} of the 10 kpc-scale lobes is $\sim 42 - 77$ Myr. This value is much larger than the typical acceleration time of CRs of a few million years.

We further compare the magnetic and hot gas pressures (derived from the Chandra observations of Li Z. et al. 2011) along the direction of the radio jets in Figure 3. Apparently, our measured magnetic pressure of the radio jets is comparable to the thermal pressure of the hot gas in the ambient medium. This suggests that

the jets in NGC 4594 could expand into the surrounding hot medium up to a distance of at least ~ 10 kpc, mainly being driven by the magnetic pressure (or the CR pressure in balance). However, it should be noted that the real viewing angle of the large-scale jets from the line-of-sight remains uncertain. If the viewing angle is significantly smaller, for instance, $\leq 25^\circ$ of the sub-pc jet as inferred from model comparisons (Hada et al. 2013), the potential beam effect and longer path-length would result in a lower value of B_{eq} and P_B , and consequently, the real radii would be longer.

We can also estimate the amount of mechanical energy required to blow out 10 kpc-scale jets in a hot medium, under the assumption of balance between the magnetic and hot gas thermal pressures at ~ 10 kpc. We assume a cylinder shape of the radio lobe, and calculate the total energy injection (assuming all from the jets) required to balance the thermal pressure of the hot gas: $E_{\text{jet}} = 4P_{\text{hot}}V$ (in analogy with the case of a bubble filled with relativistic plasma in Allen et al. 2006), where V is the volume of the radio lobe. Assuming that the jets propagate at the sound speed ($c_s \sim 400$ km s $^{-1}$) of a $kT \sim 0.6$ keV hot medium, the timescale to form a 10 kpc-scale lobe would be ~ 18 Myr. This dynamical timescale is significantly shorter than the synchrotron cooling timescale of the CR electrons. Therefore, the radiative loss of the CR electrons is in general energetically unimportant for the formation of the radio lobes. We can then calculate the required average jet power: $Q_{\text{jet}} = E_{\text{jet}}/t$, where t is the dynamical timescale. Our derived E_{jet} is $\sim 10^{55}$ ergs, and Q_{jet} is 2.7×10^{40} ergs s $^{-1}$.

As introduced above, NGC 4594 is an unusually X-ray bright SF inactive field disk galaxy, although the X-ray radiation efficiency (η , defined as the fraction of supernova (SN) energy injection released as X-ray radiation) is still far below unity (Li & Wang 2013a,b). For example, it is about two orders of magnitude X-ray brighter than the similar massive early-type SF inactive isolated disk galaxy NGC 3115 (e.g., Li J. et al. 2011; Wong et al. 2011). The high η of NGC 4594 thus cannot be explained with its SF activity or the large-scale environment.

In this paper, we for the first time discover the ~ 10 kpc scale radio lobes in NGC 4594, and link them to the smaller scale AGN jets. We further show that the jet driven outflow could be in pressure balance with the ambient hot medium at ~ 10 kpc scale. This apparently indicates the jet could provide additional energy injection,

which may contribute to the enhanced X-ray emission (the estimated jet power above, although partially from the X-ray data, is indeed one order of magnitude higher than the observed X-ray luminosity). However, caution should be made that an increased AGN jet energy injection does not necessarily lead to increased X-ray emission. Hydrodynamic simulations indicate that AGN jets heat the ambient diffuse gas, redistribute it to larger distances, and thus tend to lower the gas density and X-ray luminosity in the long run (e.g., Guo et al. 2018; Bourne & Yang 2023). However, during the early stage of a jetted AGN outburst, the jet-induced bow shock sweeps up the ambient hot gas, significantly increasing the gas density in the shock downstream and thus potentially increasing the total X-ray luminosity. This effect may be stronger in galaxies such as NGC 4594 than in more massive galaxy clusters.

1 Y.Y. acknowledges support from the National Natu-
 2 ral Science Foundation of China (NSFC) through the
 3 grant 12203098 and the Shanghai Sailing Program
 4 (19YF1455500). Both Y.Y. and J.T.L. acknowledge the
 5 support from the NSFC through the grants 12273111
 6 and 12321003, and also the science research grants from
 7 the China Manned Space Project. Z.L. acknowledges
 8 support by the National Key Research and Develop-
 9 ment Program of China (No. 2022YFF0503402) and the
 10 National Natural Science Foundation of China (grant
 11 12225302). T.W. acknowledges financial support from
 12 the grant CEX2021-001131-S funded by MCIU/AEI/
 13 10.13039/501100011033, from the coordination of the
 14 participation in SKA-SPAIN, funded by the Ministry
 15 of Science, Innovation and Universities (MCIU). F.G.
 16 thanks the support by the Chinese Academy of Sciences
 17 under grant YSBR-061 and Shanghai Pilot Program for
 18 Basic Research - Chinese Academy of Science, Shanghai
 19 Branch (JCYJ-SHFY-2021-013). Research in this field
 20 at AIRUB is supported by Deutsche Forschungsgemein-
 21 schaft SFB1491.

Facilities: VLA(NRAO)

Software: CARTA (Comrie et al. 2021), CASA (CASA Team et al. 2022),

REFERENCES

- Allen, S. W., Dunn, R. J. H., Fabian, A. C., et al. 2006, MNRAS, 372, 21. doi:10.1111/j.1365-2966.2006.10778.x
- Beck, R. & Krause, M. 2005, Astronomische Nachrichten, 326, 414. doi:10.1002/asna.200510366

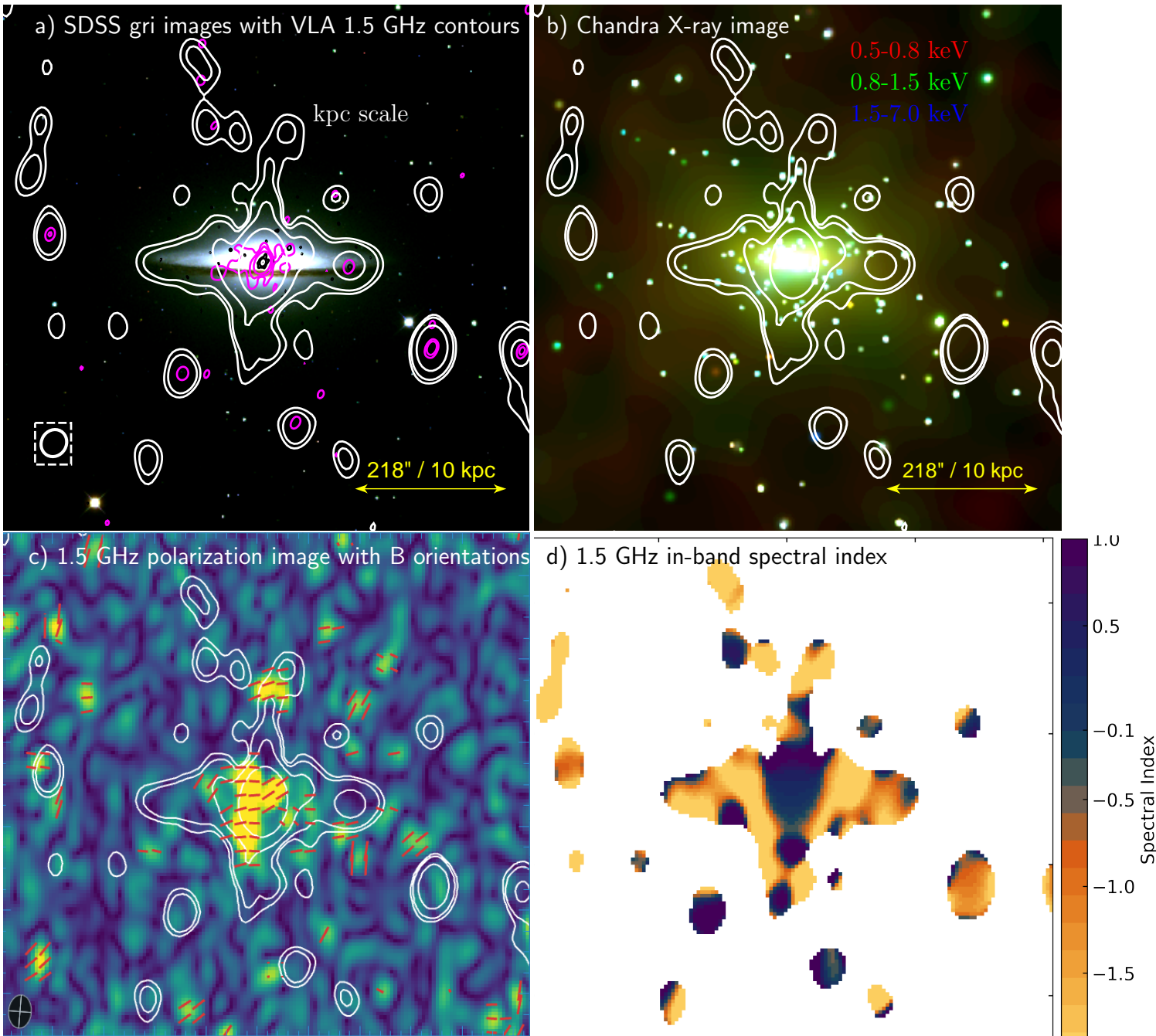


Figure 1. **a)** colour composite image of the global morphology of M 104, created by stacking images from the Sloan Digital Sky Survey (SDSS) in the g, r, and i filters. The g filter is shown in blue, while the r and i filters are shown in green and red, respectively. The white VLA 1.5-GHz D-configuration contours are at levels $\text{RMS } 45 \mu\text{Jy beam}^{-1} \times [3, 5, 15, 100]$, Zoomed-in images of the central region are shown in Figure 2. The resolution (beam size $48'' \times 33''$) of the VLA data is presented in the lower left white rectangle. **b)** Chandra X-ray tricolour image (Li Z. et al. 2011) with the same white contours. **c)** The same contours and magnetic field (B) orientations superimposed on the polarization image. The B segments have been cut off at 3σ , the RMS of the polarization image is $35 \mu\text{Jy beam}^{-1}$. This image has not been corrected for Faraday rotation. **d)** VLA 1.5 GHz D-configuration in-band spectral index. These four images show the same field of view.

Table 1. Information of M104 observations and Images

Frequency	1.5 GHz (L band)			6.0 GHz (C band)		
	Array	D ^a	C ^a	B ^a	D ^a	C ^a
Date of observations		2011-Dec-30	2012-Mar-30	2011-Mar-17	2011-Dec-19 2014-Jun-24	2012-Feb-14
Total bandwidth (MHz)		512	512	512	2048	2048
Obs. time on M104 (min) ^b		19	41	41	73	180
Flux calibrator ^c		3C286	3C286	3C286	3C286	3C286
Phase (secondary) calibrator ^d		J1246-0730	J1246-0730	J1248-1959	J1246-0730	J1246-0730
Zero-pol calibrator ^e		J1407+2827	J1407+2827	J1407+2827	J1407+2827	J1407+2827
uv weighting ^f		Briggs robust=0	Briggs robust=0	Briggs robust=0	Briggs robust=0	Briggs robust=0
I image						
Synth. beam ^g ($'' \times ''$, \circ)		47.9 \times 32.6, -4.6	14.9 \times 10.1, -21.5	4.4 \times 3.2, -14.0	13.3 \times 8.9, 1.1	3.9 \times 2.6, -3.3
RMS ^h (μ Jy beam ⁻¹)		45	30	20	18	5
$S_{core} \pm \sigma^i$ (mJy)		84.1 \pm 0.7	83.1 \pm 0.8	71.6 \pm 0.2	123.7 \pm 0.2	127.2 \pm 0.2
Fitting size ^j		48.7 \times 33.2, 175.5	15.2 \pm 10.2, 158.6	4.4 \times 3.3, 165.6	13.4 \pm 9.0, 1.1	3.9 \pm 2.6, -3.3

NOTE— ^a project ID: 10C-119; ^b Total observing time on the target galaxy before flagging; ^c Primary flux calibrator source used to calibrate bandpass and to determine the absolute position angle for polarization; ^d Secondary gain calibrator with < 3% amplitude closure errors expected in all array configurations and both bands; ^e Zero-polarization calibrator used to determine instrumental polarization leakage terms; ^f Robust = 0 used in CASA clean task; ^g Synthesized beam FWHM of major and minor axis, and position angle; ^h root-mean-square error (RMS) manually measured in emission-free region on each image; ⁱ Flux densities of the total intensity emission in the nuclear region; ^j Component size determined by fitting with 2D fit tool, convolved with beam.

Table 2. Measuring Results

Config.	scale	l	R	S	$\alpha_{in-band}$	B_{eq}	P_B	t_{syn}
(1)	(2)	($''$ /kpc)	($''$ /kpc)	(mJy)	($S \propto \nu^\alpha$)	(μ G)	(10^{-12} dyn cm ⁻²)	(Myr)
		(3)	(4)	(5)	(6)	(7)	(8)	(9)
L band (center frequency 1.5 GHz)								
B	north hundreds pc	6.0-13.0/0.32	3.2/0.15	0.22 \pm 0.03	-1.5 \pm 1.5	26	27	6
	south hundreds pc	3.0-6.0/0.14	3.0/0.14	0.11 \pm 0.02	-1.5 \pm 1.5	28	31	6
C	north sub-kpc	16.8-28.6/0.54	10.8/0.50	0.99 \pm 0.04	-1.4 \pm 1.2	19	14	10
	south sub-kpc	17.2-19.0/0.08	13.9/0.64	1.01 \pm 0.03	-2.4 \pm 1.5	28	32	6
D	north kpc	49.1-213.4/7.56	36.4/1.67	2.39 \pm 0.12	-1.5 \pm 0.9	7	2	42
	south kpc	51.7-175.4/5.69	65.0/2.99	1.79 \pm 0.13	-1.2 \pm 1.0	5	1	77
C band (center frequency at 6 GHz)								
C	north hundreds pc	5.3-8.2/0.13	1.7/0.08	0.13 \pm 0.01	-0.9 \pm 1.2	51	105	1
	south hundreds pc	5.3-9.3/0.18	3.2/0.15	0.21 \pm 0.01	-1.2 \pm 1.0	42	71	1
D	north sub-kpc	19.7-45.2/1.17	10.5/0.48	0.28 \pm 0.03	-0.7 \pm 1.1	13	7	9
	south sub-kpc	18.4-41.2/1.05	10.9/0.50	0.23 \pm 0.03	-0.6 \pm 1.0	13	7	9

NOTE—Column 1: VLA observing configurations; Column 2: the scale of the extended structure; Column 3: the closest and farthest radial distance of the radio extended structures from the center of M104 ($''$), and the length of the radio extended structures in kpc; Column 4: the path length of the northern radio extended structure, which we assumed to be equal to its width; Column 5: flux density of the northern/southern radio extended structure; Column 6: in-band spectral index; Column 7: equipartition magnetic field B of the radio extended structure (estimated by the revised equipartition formula of Beck & Krause (2005) with the corresponding flux density and in-band spectral index; Column 8: magnetic pressure, P_B ; Column 9: the synchrotron half-power lifetime of CR electrons (Beck & Wielebinski 2013);

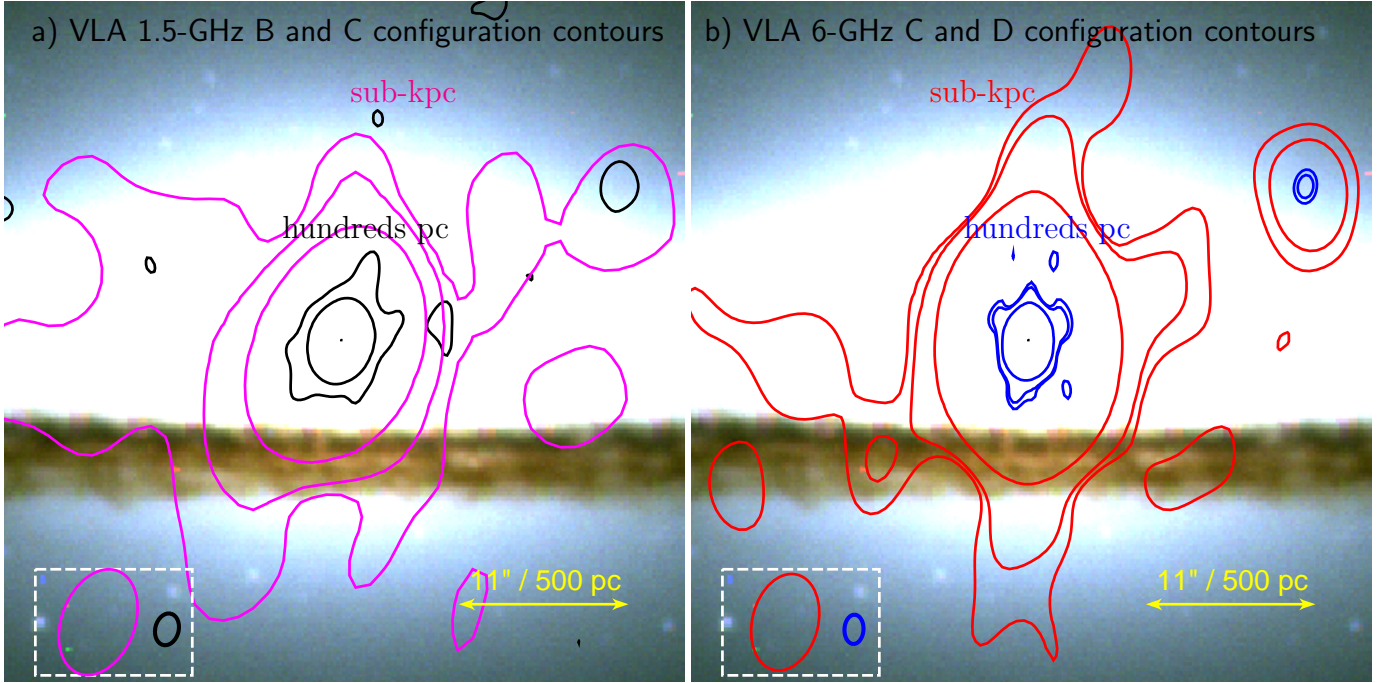


Figure 2. Zoomed-in images of the central region of Figure 1a. **a)** The magenta contours of the VLA 1.5-GHz C-configuration observation are at levels $\text{RMS } 30 \mu\text{Jy beam}^{-1} \times [7, 20, 100]$, the black contours of the VLA 1.5-GHz B-configuration observation are at levels $\text{RMS } 20 \mu\text{Jy beam}^{-1} \times [3, 30]$. The beam size are respectively $15'' \times 10''$ and $4'' \times 3''$ in the lower left white rectangle. **b)** the red contours of the VLA 6-GHz D-configuration observation are at levels of $\text{RMS } 18 \mu\text{Jy beam}^{-1} \times [3, 5, 30]$, the blue contours of the VLA 6-GHz C-configuration observations are at the levels $\text{RMS } 5 \mu\text{Jy beam}^{-1} \times [10, 18, 180]$. The beam size are respectively $13'' \times 9''$ and $4'' \times 3''$ in the lower left white rectangle.

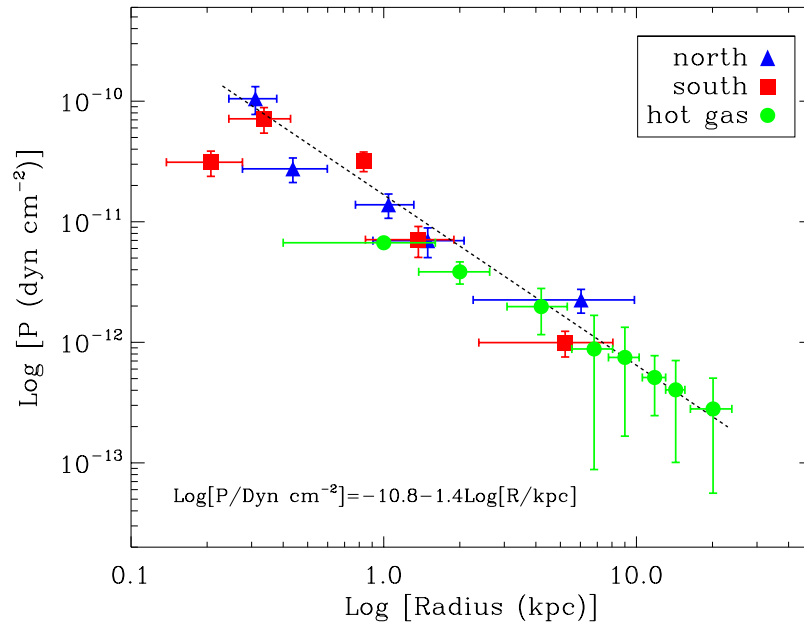


Figure 3. The magnetic pressure and hot gas pressure along the radio jets: The x-axis indicates the distance from the center of M104 on the sky plane. The blue triangles indicate the magnetic pressure of the northern jet, the red squares are that of the southern jet, and the green circles show the profile of the hot gas pressure (hot gas data are from Fig. 9 of Li Z. et al. (2011)), the dashed line is a linear fit of the red and blue data points with a slope of -1.4.

- Beck, R. & Wielebinski, R. 2013, *Planets, Stars and Stellar Systems. Volume 5: Galactic Structure and Stellar Populations*, 641. doi:10.1007/978-94-007-5612-0_13
- Bourne, M. A., & Yang, H.-Y. K. 2023, *Galaxies*, 11, 73
- CASA Team, Bean, B., Bhatnagar, S., et al. 2022, *PASP*, 134, 114501. doi:10.1088/1538-3873/ac9642
- Comrie, A., Wang, K.-S., Hsu, S.-C., et al. 2021, Zenodo
- Fanaroff, B. L. & Riley, J. M. 1974, *MNRAS*, 167, 31P. doi:10.1093/mnras/167.1.31P
- Gallimore, J. F., Axon, D. J., O’Dea, C. P., Baum, S. A., & Pedlar, A. 2006, *AJ*, 132, 546
- Guo, F., Duan, X., & Yuan, Y.-F. 2018, *MNRAS*, 473, 1332
- Hardcastle, M. 2018, *Nature Astronomy*, 2, 273. doi:10.1038/s41550-018-0424-1
- Hada, K., Doi, A., Nagai, H., et al. 2013, *ApJ*, 779, 6
- Harrison, C. M., Costa, T., Tadhunter, C. N., et al. 2018, *Nature Astronomy*, 2, 198. doi:10.1038/s41550-018-0403-6
- Irwin, J., Beck, R., Benjamin, R. A., et al. 2012, *AJ*, 144, 43
- Irwin, J., Beck, R., Benjamin, R. A., et al. 2012, *AJ*, 144, 44. doi:10.1088/0004-6256/144/2/44
- Irwin, J. A., Schmidt, P., Damas-Segovia, A., et al. 2017, *MNRAS*, 464, 1333. doi:10.1093/mnras/stw2414
- Irwin, J., Wiegert, T., Merritt, A., et al. 2019, *AJ*, 158, 21. doi:10.3847/1538-3881/ab25f6
- Jiang, Y., Li, J.-T., Gao, Y., et al. 2023, *MNRAS*. doi:10.1093/mnras/stad2473
- Karachentsev, I. D., Makarova, L. N., Brent Tully, R., et al. 2020, *A&A*, 643, A124.
- Kennicutt, R. C., Calzetti, D., Aniano, G., et al. 2011, *Publications of the Astronomical Society of the Pacific*, 123, 1347
- Kormendy, J. 1988, *ApJ*, 335, 40. doi:10.1086/166904
- Kormendy, J., Bender, R., Ajhar, E. A., et al. 1996, *ApJL*, 473, L91. doi:10.1086/310399
- Kharb, P., Srivastava, S., Singh, V., et al. 2016, *MNRAS*, 459, 1310. doi:10.1093/mnras/stw699
- Krause, M., Wielebinski, R., & Dumke, M. 2006, *A&A*, 448, 133. doi:10.1051/0004-6361:20053789
- Kormendy, J. & Ho, L. C. 2013, *ARA&A*, 51, 511. doi:10.1146/annurev-astro-082708-101811
- Li, Z., Jones, C., Forman, W. R., et al. 2011, *ApJ*, 730 (IOP Publishing), 84
- Li, J.-T., Wang, Q. D., Li, Z., et al. 2011, *ApJ*, 737, 41. doi:10.1088/0004-637X/737/1/41
- Li, J.-T. & Wang, Q. D. 2013, *MNRAS*, 428, 2085. doi:10.1093/mnras/sts183
- Li, J.-T. & Wang, Q. D. 2013, *MNRAS*, 435, 3071. doi:10.1093/mnras/stt1501
- McNamara, B. R. & Nulsen, P. E. J. 2007, *ARA&A*, 45, 117. doi:10.1146/annurev.astro.45.051806.110625
- McQuinn, K. B. W., Skillman, E. D., Dolphin, A. E., et al. 2016, *AJ*, 152, 144.
- Mezcua, M., & Prieto, M. A. 2014, *ApJ*, 787, 62
- Perley, R. A. & Butler, B. J. 2013, *ApJS*, 204, 19.
- Rubin, V. C., Burstein, D., Ford, W. K., Jr., & Thonnard, N. 1985, *ApJ*, 289, 81
- Seta, A. & Beck, R. 2019, *Galaxies*, 7, 45. doi:10.3390/galaxies7020045
- Vargas, C. J., Waltherbos, R. A. M., Rand, R. J., et al. 2019, *ApJ*, 881, 26
- Wong, K.-W., Irwin, J. A., Yukita, M., et al. 2011, *ApJL*, 736, L23. doi:10.1088/2041-8205/736/1/L23
- Wagner, S. J., Dettmar, R. J., & Bender, R. 1989, *A&A*, 215, 243
- Wiegert, T., Irwin, J., Miskolczi, A., et al. 2015, *AJ*, 150, 81. doi:10.1088/0004-6256/150/3/81
- Yang, Y., Irwin, J., Li, J., et al. 2022, *ApJ*, 927, 4. doi:10.3847/1538-4357/ac4ae7